



FULL LENGTH ARTICLE

Numerical investigation on characteristics of interfacial wave of liquid film in gas–liquid two-phase flow using OpenFOAM



Xiaoqi MA, Yueshe WANG*, Jiaming TIAN

State Key Laboratory of Multiphase Flow in Power Engineering, Xi'an Jiaotong University, Xi'an 710049, China

Received 31 January 2023; revised 6 March 2023; accepted 28 April 2023

Available online 20 August 2023

KEYWORDS

Interfacial wave;
Gas-liquid;
Two-phase flow;
VOF model;
OpenFOAM

Abstract Liquid film cooling as an advanced cooling technology is widely used in space vehicles. Stable operation of liquid film along the rocket combustion inner wall is crucial for thermal protection of rocket engines. The stability of liquid film is mainly determined by the characteristics of interfacial wave, which is rarely investigated right now. How to improve the stability of thin film has become a hot spot. In view of this, an advanced model based on the conventional Volume of Fluid (VOF) model is adopted to investigate the characteristics of interfacial wave in gas–liquid flow by using OpenFOAM, and the mechanism of formation and development of wave is revealed intuitively through numerical study. The effects from gas velocity, surface tension and dynamic viscosity of liquid (three factors) on the wave are studied respectively. It can be found that the gas velocity is critical to the formation and development of wave, and four modes of droplets generation are illustrated in this paper. Besides, a gas vortex near the gas–liquid interface can induce formation of wave easily, so changing the gas vortex state can regulate formation and development of wave. What's more, the change rules of three factors influencing on the interfacial wave are obtained, and the surface tension has a negative effect on the formation and development of wave only when the surface tension coefficient is above the critical value, whereas the dynamic viscosity has a positive effect in this process. Lastly, the maximum height and maximum slope angle of wave will level off as the gas velocity increases. Meanwhile, the maximum slope angle of wave is usually no more than 38°, no matter what happens to the three factors.

© 2023 Production and hosting by Elsevier Ltd. on behalf of Chinese Society of Aeronautics and Astronautics. This is an open access article under the CC BY-NC-ND license (<http://creativecommons.org/licenses/by-nc-nd/4.0/>).

* Corresponding author.

E-mail address: wangys@mail.xjtu.edu.cn (Y. WANG).

Peer review under responsibility of Editorial Committee of CJA.



Production and hosting by Elsevier

1. Introduction

Gas-liquid two-phase flow is widely encountered in many different industrial applications, like nuclear power plants, oil pipelines, rocket combustion chambers, and so on. Especially for a space rocket engine, the technique of liquid film cooling is extensively applied to protect the chamber wall.^{1–4} In this

process, there is a typical gas–liquid flow in a chamber, and the state of liquid film flow is crucial to reliable operation of the combustion chamber. When liquid film is injected to flow along the inner wall of a chamber, the film will interact with the combustion core gas. The interface between gas and liquid will become unstable, which will induce an obvious interfacial wave, and even lots of droplets will be generated. The instability of liquid film affects its cooling effectiveness dramatically, so how to improve the stability of film is necessary for thermal protection of a combustion chamber.^{5–9} In this situation, the interfacial wave in film flow plays an important role in the mass, momentum, and energy transfer process between gas and liquid film, and thus an investigation on the characteristics of interfacial wave is crucial to reveal the mechanism of wave formation and development.

The characteristics of interfacial wave are mainly determined by its geometrical shape, which mainly involves the height, slope angle, and celerity of wave. Thus, a clear interface between gas and liquid is important to investigate interfacial wave, which also puts forward a high request to research methods. It's difficult to obtain the characteristic parameters of interfacial wave in previous experimental studies conducted by some researchers.^{10–13} Only the prediction correlations of droplets entrainment fraction were obtained. The characteristics of interfacial wave were rarely obtained, and a clear interface was hardly captured intuitively. Consequently, the mechanism of wave formation and development is not clear, and the gas velocity or liquid property on how to affect the stability of film flow is not illustrated, which is the purpose of the current research.

The mass, momentum, and energy transfers between gas and liquid are significantly altered by the behaviors of interfacial wave. Cuadros (2019),¹⁴ He (2022),¹⁵ and Rivera (2022)¹⁶ et al. have conducted similar experiments to explore the behaviors of interfacial wave based on the conductivity-based technique respectively, which improves the knowledge of interfacial wave characteristics. They all measured the film thickness and the major characteristic of interfacial wave using a non-intrusive instrument, a conductance probe. The physical phenomenon on which this device is based is the change in the electrical conductivity between gas and liquid. The experimental raw data was a voltage signal, which needed to be processed by some complicated methods, and then the film thickness and other characteristic parameters were concluded indirectly.¹⁴

The major conclusions obtained by Cuadros et al. (2019)¹⁴ were that the evolution of liquid film thickness was in the direct proportionality with the liquid film flow rate and the inverse proportionality with the gas flow rate. Besides, Cuadros et al.¹⁴ proposed the prediction correlations of liquid film thickness, wave amplitude, and wave frequency.

He et al. (2022)¹⁵ confirmed that the interactions between turbulent gas flow and liquid film were found to be pertinent for the inception of ultrafast-evolved ripple waves with irregular shapes in terms of different characteristic sizes. They found that millisecond-scale ripple waves induced by turbulent gas as precursors experienced a series of second-scale self-convolution to evolve into a random distribution of disturbance waves. At last, they predicted the time interval and the disturbance waves height statistically by gamma distributions.

Rivera et al. (2022)¹⁶ conducted experiments in free falling and downward cocurrent annular flows. They found that the liquid film thickness increased as the liquid Reynolds number increasing; however, it decreased more strongly with the gas

Reynolds number, which was similar to Cuadros et al.'s finding¹⁴ in essence. They developed new correlations for liquid film thicknesses, disturbance wave and disturbance wave frequencies in terms of dimensionless numbers, and their aim was to provide more general relations.

However, interface information was easily affected by the conductivity-based technique, which was because probes were usually discontinuously located along the test section in the aforementioned experiments, and all the experimental data was from these interspaced probes. Thus, it was hard to get continuous interface information. In addition, the calculation error caused by different post-processing methods of raw data was inevitable.

In order to capture the behaviors of interfacial wave more intuitively, Wijayanta et al.¹⁷ conducted an experimental study using image processing techniques to investigate the effects of liquid physical properties on the liquid film thickness, wave frequency, and wave velocity in gas–liquid flow in a horizontal pipe. A high-speed video camera was used to take visual data which was then processed by developed image processing techniques to obtain the time-series data of the liquid film thickness. The Probability Distribution Function (PDF) and Discrete Wavelet Transform (DWT) were used to analyze the time series of the liquid film thickness. They studied the formation and development of interfacial wave preliminarily, and found that superficial gas velocity, liquid viscosity, and liquid surface tension were important parameters in the gas–liquid flow. However, the interface between gas and liquid was smoothed artificially during image processing, and the detailed information on the interfacial wave was ignored inevitably. Besides, the interfacial stress and the velocity and vorticity of the flow field were not investigated.

Due to the limitation of experimental observation, it's difficult to capture detailed information about interfacial wave in experiments. Some theoretical analysis^{18–20} and numerical simulation studies on interfacial wave have become the focus in recent years. Especially for wave formation and development, a numerical method can make it easier to capture interface information. Rana (2016),²¹ Stel (2022),²² and Ramadan (2021)²³ et al. developed a computational fluid dynamics model respectively to investigate the behavior of gas–liquid two-phase flow. Rana et al.²¹ investigated film wrapping and liquid entrainment by the rotation of a horizontal roller which was placed between the gas–liquid interface by a numerical method. They found the entrainment pattern at different rotational speeds and obtained detailed information at the interface. Besides, they showed that the viscosity played a major role in deciding the azimuthal wrap thickness. Stel et al.²² presented a numerical study of performance characteristics and flow dynamics of a centrifugal rotor operating with gas–liquid flow, in which an Euler-Euler polydispersed model was adopted to further analyze flow patterns and relevant gas–liquid flow quantities, and the results of their study could help to understand the gas–liquid flow behavior in centrifugal rotors. Rana et al.'s and Stel et al.'s findings were only applicable to gas–liquid flow on the surface of a solid roller. Ramadan and Park²³ investigated numerically gas–liquid two-phase flow in a T-junction microchannel, and the Volume of Fluid (VOF) method was adopted. Three flow regimes (squeezing, dripping, and jetting) were observed. The development of an interface between gas and liquid was well captured, and some very interesting phenomena could be found, which was hardly

observed in previous experimental studies. However, the influences from gas velocity, surface tension, and dynamic viscosity on the gas–liquid flow weren't considered in the above research, and the characteristics of interfacial wave were also not explained.

Based on the above analysis, there have been few reports on the characteristics of interfacial wave in a liquid film flow, and the formation and development process of interfacial wave is still unknown, especially that the influences from different gas momentum and different liquid properties such as surface tension and viscosity on gas–liquid interface and how to improve the stability of liquid film are still uninvestigated. Consequently, it is very necessary to conduct a study in this aspect, and the above numerical method to investigate gas–liquid flow can give a good reference in gas–liquid two-phase flow, so the numerical method is adopted in present investigation, which is proper and effective to reveal the interaction mechanism between gas and liquid.

2. Physical and mathematic model

2.1. Physical model

A schematic picture of horizontal gas–liquid flow is shown in Fig. 1. The diameter and length of the pipe are 10 mm and 200 mm, respectively. In order to study wave formation and development more intuitively, the initial film thickness is assumed to be half of the pipe diameter. The velocity of gas and liquid properties play an important role in the gas–liquid two-phase flow. Thus, these parameters are all investigated to reveal the interaction mechanism between gas and liquid more comprehensively in present study.

2.2. Governing equations and discretization schemes

In a horizontal gas–liquid pipe, the profile of gas–liquid interface is calculated using the solver interFOAM in OpenFOAM. The continuity and momentum equations of two-phase immiscible fluids (gas and liquid) for a two-dimensional, laminar and unsteady flow are written as follows:

$$\frac{\partial \rho}{\partial t} + \nabla \cdot (\rho \mathbf{u}) = 0 \quad (1)$$

$$\frac{\partial \rho \mathbf{u}}{\partial t} + \nabla \cdot (\rho \mathbf{u} \mathbf{u}) = -\nabla p + \nabla \cdot \boldsymbol{\tau} + \rho g + \mathbf{F}_\sigma \quad (2)$$

where ρ is the density of the fluid, \mathbf{u} is the velocity vector, p is the pressure, $\boldsymbol{\tau}$ is the shear stress, t is the time, \mathbf{g} is the gravitational acceleration, and \mathbf{F}_σ is the surface tension.

The term $\boldsymbol{\tau}$ is induced by the deformation tensor of the viscous fluid, which can be written as

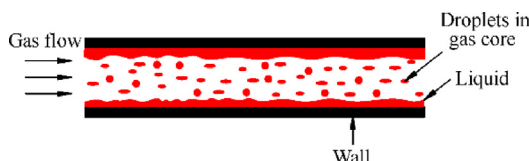


Fig. 1 Schematic representation of gas–liquid flow in a horizontal pipe.

$$\boldsymbol{\tau} = 2\mu \mathbf{D} \quad (3)$$

The viscous stress tensor can be written as

$$\mathbf{D} = (\nabla \mathbf{u} + \nabla \mathbf{u}^T)/2 \quad (4)$$

The term \mathbf{F}_σ as a source term is added to the momentum Eq. (2). In OpenFOAM, the Continuum Surface Force (CSF) model is used to represent the effect of surface tension as a continuous volumetric force acting within the interface region. It can be written as

$$\mathbf{F}_\sigma = \sigma \kappa \nabla \alpha \quad (5)$$

$$\kappa = -\nabla \cdot \left(\frac{\nabla \alpha}{|\nabla \alpha|} \right) \quad (6)$$

where σ is the surface tension coefficient, κ is the curvature at the interface, and $\nabla \alpha$ is the phase fractional gradient.

The VOF method is used to track the interface between gas and liquid. This method employs the volume fraction, α , to identify the phase. The amount of fluid in each cell is represented by α , varying between 0 and 1. If only gas is present in a cell, α equals 0, whereas α equals 1 if the cell is filled with liquid, while α between 0 and 1 represents the interface. Thus, the solution of α is very crucial to determine the gas–liquid interface. Based on this definition of volume fraction, the density and viscosity of fluid can be written as

$$\rho = \alpha \rho_f + (1 - \alpha) \rho_g \quad (7)$$

$$\mu = \alpha \mu_f + (1 - \alpha) \mu_g \quad (8)$$

The equation of phase function can be concluded from Eq. (1) and Eq. (7) for incompressible flow as follows:

$$\frac{\partial \alpha}{\partial t} + \mathbf{u} \cdot \nabla \alpha = 0 \quad (9)$$

The conventional VOF model is solved by combining Eq. (1) to Eq. (9), and this model has been adopted in commercial software such as Fluent and CFX. Results show that the sharpness of interface is low,²⁴ so it is hard to capture the characteristics of interfacial wave.

In order to obtain the detailed information of interfacial wave, OpenFOAM uses an advanced model based on the conventional VOF. In this model, an artificial convection term is used to compress the volume fraction at the interface to depress the interface fuzziness caused by numerical diffusion. This model provides a sharper interface resolution²⁵ and can capture the actual interface more intuitively in gas–liquid flow, which is valuable to investigate the characteristics of interfacial wave, and thus we adopt this advanced model in current research. The improved equation of phase function can be written as

$$\frac{\partial \alpha}{\partial t} + \mathbf{u} \cdot \nabla \alpha + \nabla \cdot [\alpha(1 - \alpha) \mathbf{u}_c] = \alpha \nabla \cdot \mathbf{u} \quad (10)$$

The third term of the left side of Eq. (10) is the artificial compression term, which does not involve the compressible flow and is only related to the flow in the normal direction of the interface between gas and liquid. \mathbf{u}_c in Eq. (10) is the compression velocity of the interface, and it can be written as

$$\mathbf{u}_c = \min [c|\mathbf{u}|, \max(|\mathbf{u}|)] \frac{\nabla \alpha}{|\nabla \alpha|} \quad (11)$$

where c is the compression factor, which is a constant. It represents no compression effect at the interface if $c = 0$, and a conservative compression for $c = 1$ adopted in present study, while enhanced compression for $c > 1$.²⁵

The PIMPLE algorithm is used for pressure–velocity coupling, which is a combination of both Pressure Implicit with Splitting of Operators (PISO) and Semi-Implicit Method for Pressure-Linked Equations (SIMPLE) algorithms. The Finite Volume Method (FVM) is applied to discrete the Navier–Stokes equations, and the Gauss integration method is used to solve in OpenFOAM.²⁶ The local linearization of the source term²⁷ is processed in present research. The central difference scheme is of second-order accuracy, but its boundedness cannot be guaranteed, whereas the upwind scheme is good, but it only has one-order accuracy. In order to overcome the disadvantages of upwind difference and center difference and ensure the accuracy of calculation, the mixed difference scheme of center difference and windward difference^{28,29} is adopted in this study. The explicit MULES (Multi-dimensional Universal Limiter with Explicit Solution) algorithm is employed with interface compression to perform interface capture through the VOF method. An adjustable time step controlled by a maximum Courant number equal to 0.5 is adopted, and the time step can be adjusted automatically during calculation.

3. Model description and validation test

3.1. Model description

The schematic of gas–liquid flow in a horizontal pipe is shown in Fig. 2, and the interaction between gas and liquid is mainly determined by the velocity difference between gas and liquid,^{30,31} so water can be assumed to be stationary initially. The gas flowed above the interface at different gas velocities along the x -axis, and the velocity was uniform at the entrance initially. The wall was in no slip boundary condition, and a standard wall function was used in present study. The region below $y = 0.005$ mm from the wall was assumed initially to be filled with liquid, where $\alpha = 1$, and the rest was full of gas. Meanwhile, the combined boundary conditions of the velocity inlet and the pressure outlet were used in the solution process. Liquid properties and initial boundary conditions are shown in Table 1 and Table 2, respectively.

The wave geometric structure and parameters are illustrated in Fig. 3, in which δ indicates the initial thickness of film, θ indicates the wave slope angle, Δh indicates the wave height, h indicates the total height of wave, h_t indicates the depth of trough, and L indicates the wave width. These geometric parameters can be obtained from calculation results through the measuring software getdata.

The wave height Δh is a significant parameter of interfacial wave, which reflects the interaction strength between gas and liquid. The velocity is an important parameter reflecting the

Table 1 Physical properties.

Item	Density (kg/m ³)	Viscosity (Pa·s)	Surface tension coefficient (N/m)
Gas (air)	1	1.48×10^{-5}	
Liquid (water)	1000	0.001	0.07

flow field information. In order to find the optimum refinement level of cells required to simulate our problem, grid independence tests were performed as shown in Table 3 and Fig. 4. It can be found that the result is still stable when the grids number is up to 77922. Thus 77922 cells are adopted in the subsequent calculations.

3.2. Validation test

To verify the interface accuracy of the calculation model, interfacial wave is simulated under different compression factors firstly. Results are shown in Fig. 5.

Fig. 5 shows that the interface is fuzzy especially for the wave crest if there is no compression effect ($c = 0$), which is caused by the numerical diffusion during the calculation, and this method is usually called conventional VOF model. On the contrary, the interface is smooth and clear when there is a compression factor ($c = 1$), that's because the compression factor can suppress the numerical diffusion and improve the interface sharpness. Bae et al.¹⁰ conducted PIV (Particle Image Velocimetry) visualization to capture the flow field of liquid in a rectangular channel, of which the width and height were 40 mm and 50 mm, respectively. Calculation was conducted under the same conditions as those of Bae et al.'s experiment. The liquid and gas Reynolds numbers were 3535 and 14333, respectively. Fig. 6 shows that the flow field calculation result agrees with the experimental result very well, while the gas–liquid interface is distinct and continuous. Besides, a comparison of the interface profile between them is shown in Fig. 7, in which the maximum deviation between them is about 14% while the average deviation is about 5%, and the average deviation can be calculated by Eq. (12). Thus, it is found that the calculation result can predict the actual interface to a great extent, and the deviation is possibly caused by an entrance effect, because actual inlet conditions are non-uniform due to the centrifugal pump supply in an experimental system, while they are uniform in current calculation.

$$\xi = \frac{1}{n} \sum_{i=1}^n \frac{y_i - y_i^*}{y_i^*} \quad (12)$$

where ξ is the average deviation, y_i is the calculation result, y_i^* is the experimental result, n is the total number of comparison points, and subscript i is the serial number of a point.

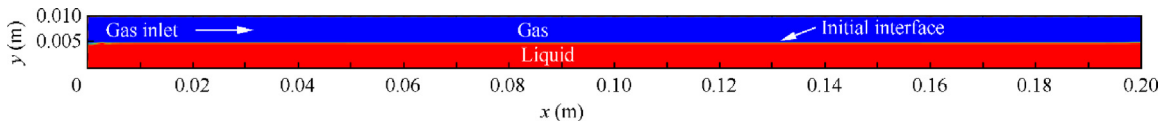
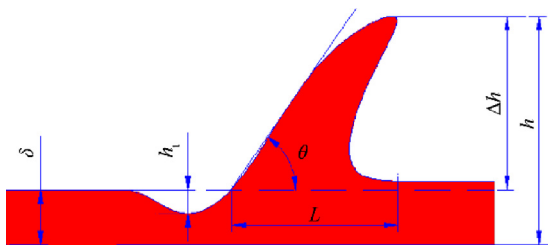


Fig. 2 Schematic of gas–liquid flow in a horizontal pipe.

Table 2 Boundary conditions.

Case	1	2	3	4	5	6
Gas inlet velocity (m/s)	5.0	5.8	6.5	7.2	8.0	10.0
Water initial velocity(m/s)	0	0	0	0	0	0
Pressure outlet (MPa)	0.1	0.1	0.1	0.1	0.1	0.1
Phase fraction α ($y > 0.005$ m)	0	0	0	0	0	0
Phase fraction α ($y \leq 0.005$ m)	1	1	1	1	1	1

**Fig. 3** Schematic diagram of structural parameters of father wave.

Based on the above analysis, the advanced method can capture the detailed information of interfacial wave, which is important for present investigation.

For further validation of the CFD model, it was compared with Belt et al.'s correlation,³² Mantilla's correlation,³³ and Alekseenko et al.'s correlation³⁰ as shown in Fig. 8. It's found that the trend of present study is consistent with those of Belt, Mantilla, and Alekseenko et al. Besides, the magnitudes were approximate to them. Thus, the advanced model can be used to conduct an investigation of gas–liquid two-phase flow in a horizontal pipe. The wave celerity is calculated by the following equation:

$$V = \frac{\Delta x}{t} \quad (13)$$

where V is the wave celerity, Δx is the displacement of the crest along the x -axis direction, and t is time.

4. Results and discussion

4.1. Different gas inlet velocities

The formation and development process of wave is crucial for studying the characteristics of interfacial wave and revealing the mechanism of droplet entrainment. Gas will drag liquid to flow when gas flows above liquid, which is because there is a velocity difference between gas and liquid, and shear stress is caused by the friction between gas and liquid. The integral of

shear stress along the surface of wave eventually forms a drag force. The drag force has an important impact on the formation and development of wave, which is influenced seriously by the velocity difference between gas and liquid. Thus, it is very necessary to conduct investigations at different gas speeds.

Fig. 9 shows that wave formation and development vary with the gas velocity, which determines the formation time and the wave scale. The time becomes shorter and the wave scale gets greater as the gas velocity increases. When gas flows above liquid, the liquid surface is dragged by the gas flowing backward, while the downstream liquid is nearly static, so as a result, the upstream liquid is continuously uplifted backward to form the first wave, which is named as father wave in our research. Meanwhile, a series of wavelets is generated after father wave due to the combined effect of gas flow and father wave development, which is named as son waves in our research. Besides, father wave is usually more obvious than son waves, and the formation of father wave precedes son waves. Thus, the formation and development of father wave is important for investigation on characteristics of interfacial wave in present research. When the gas velocity is within the range of 5.0 m/s to 5.8 m/s, interfacial wave starts to form, and the wave width L gets shorter as it moves away from the gas entrance, which is because the downstream liquid surface is less affected by gas. The interface between gas and liquid is relatively flat on the whole, and there is no droplet entrainment in gas–liquid flow, as shown in Figs. 9(a) and (b). This phenomenon is due to that the surface tension can suppress the shear stress induced by gas, and the interface can remain smooth and continuous. The formation and development of father wave are very rapid when the gas velocity is above 5.8 m/s, as shown in Figs. 9(c) and (d). The upwind of father wave is elongated and uplifted rapidly, and a crest is formed. The surface tension and gravity can't suppress the shear stress, which will cause the top of father wave to be cut off by the shear stress. Consequently, droplets will be generated, and the rest of father wave will be pushed down and hit the downstream liquid surface under the influence of gas, which will generate secondary droplets into the core gas. The hitting will destroy the downstream liquid surface rapidly,

Table 3 Grid independence tests (gas velocity: 7.2 m/s, $t = 0.1$ s).

Grids number	15632	27325	53268	64897	77922
Wave height Δh (mm)	1.91	1.95	1.98	2.00	2.00

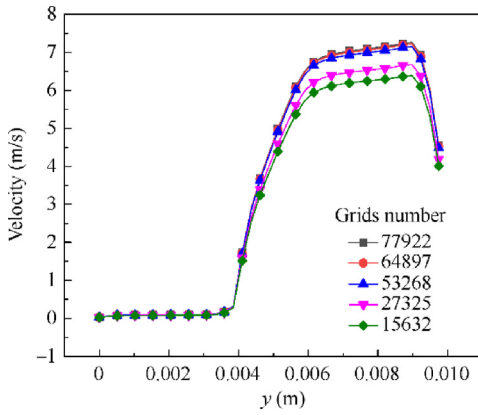


Fig. 4 Velocity distributions on cross-section $x = 0.02$ m under different grids numbers (gas velocity: 7.2 m/s, $t = 0.105$ s).

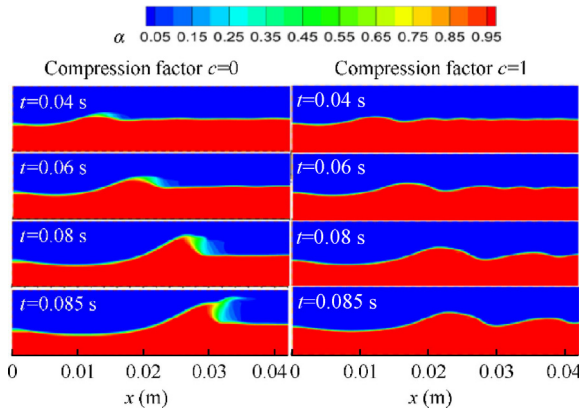


Fig. 5 Compression effect (gas velocity: 7.2 m/s).

which also disrupts the downstream wave pattern, and gas will also be sucked into liquid to form bubbles during this period. The bubbles in liquid roll and deform with the movement of the fluid and eventually burst, which also generates droplets into the core gas. According to the above analysis, droplets are generated mainly by the following four modes: cutting off from gas, hitting from the wave body, droplets impingement, and bubbles burst, all of which are shown in Fig. 10. These four phenomena usually coexist, so some entrainment rate correlations^{18–20} only based on the cutting off mode could not reflect the actual droplets entrainment in gas–liquid flow.

To further reveal the mechanism of droplets entrainment, the relations between the gas Reynolds number, Weber number, and development of wave are shown in Fig. 11. It can be found that the gas velocity is positively associated with

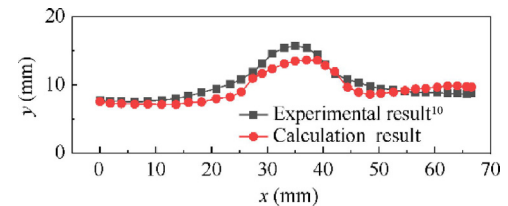


Fig. 7 Comparison with experimental interface profile.

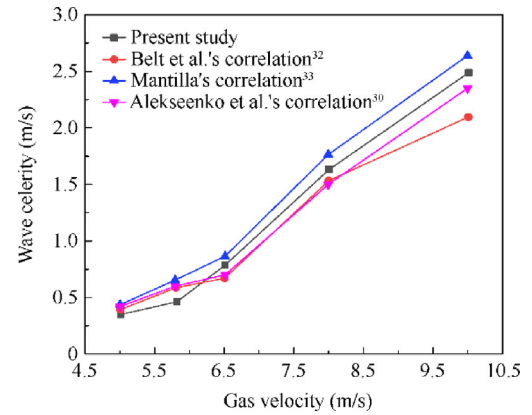


Fig. 8 Validation tests.

Re_g , We_g , and wave celerity. Re_g and We_g corresponding to the onset of droplets entrainment are 4400 and 6, respectively, in horizontal gas–liquid two-phase flow. The wave celerity increases rapidly after these values, which is caused by increasing drag force as the gas velocity increases. The phase, velocity, and shear stress contours are shown in Fig. 12, and the shear stress increases with the growth of the gas velocity along the windward side of wave, thus the liquid is elongated like a small mountain. In Fig. 13, there is a reversed distribution trend between surface tension and shear stress along the windward side of wave on the whole. The shear stress increases while the surface tension decreases, and the two forces are equal at $x = 0.0263$ m. The shear stress exceeds the surface tension after $x = 0.0263$ m, and the difference between them is greatest near the top of wave. When this difference overcomes the gravity of a certain volume of liquid near the crest, the liquid will be cut off to induce an occurrence of liquid droplets entrainment. What's more, the shear stress firstly increases gradually before $x = 0.028$ m and then increases dramatically, which is because the gas velocity is greatest near the crest. The highest shear stress region is located at the top of wave (corresponding to Fig. 12(c)), where the interaction between gas and liquid is

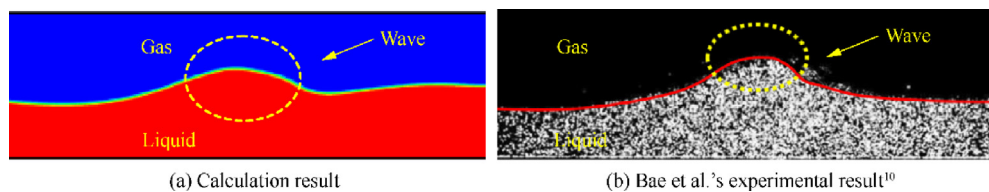


Fig. 6 Comparison between calculation result and Bae et al.'s experimental result.¹⁰

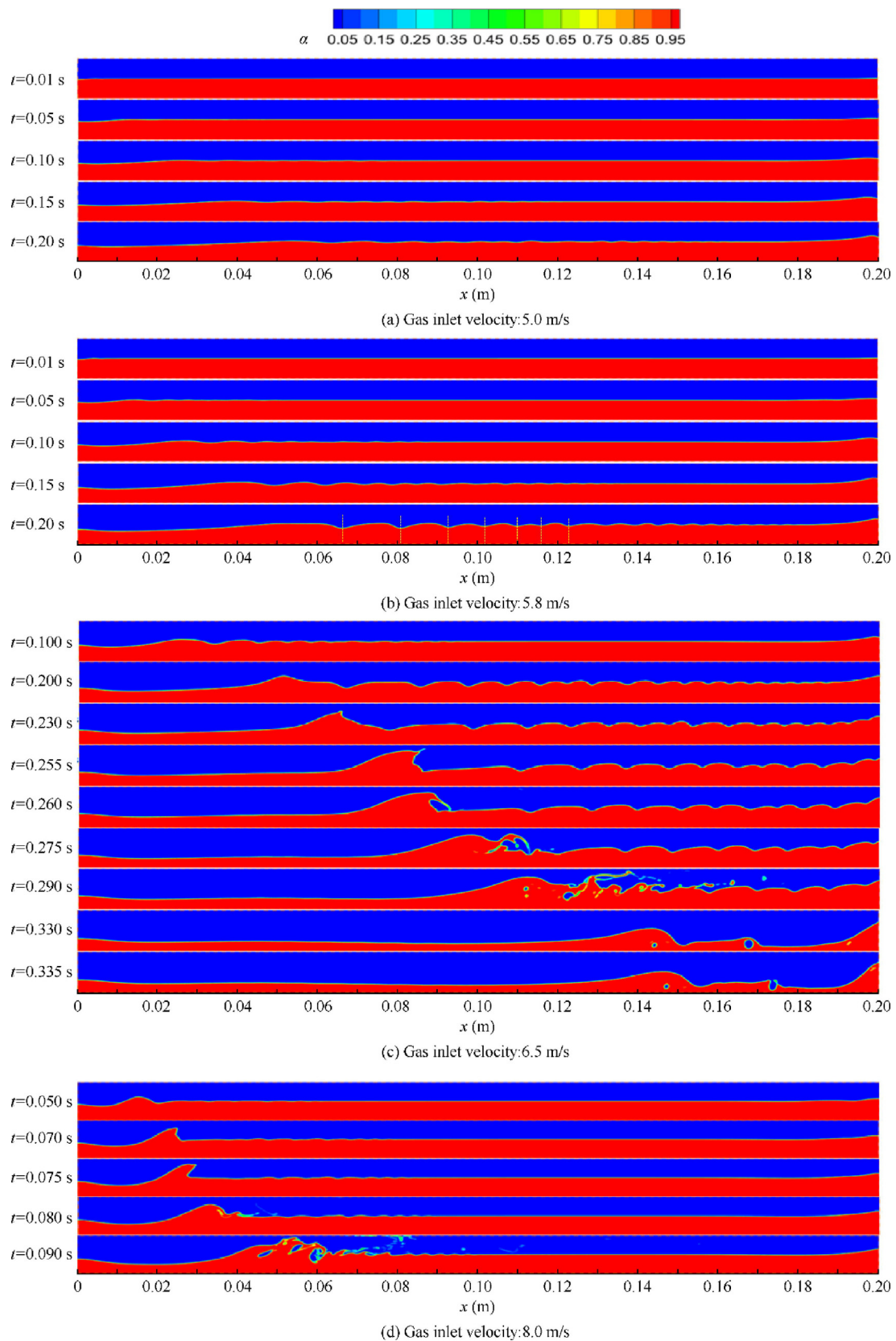


Fig. 9 Formation and development of wave at different gas velocities.

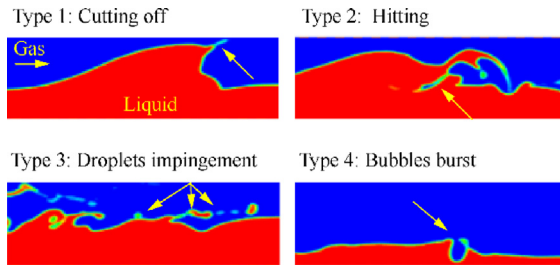


Fig. 10 Different droplets generation modes in horizontal gas–liquid two-phase flow.

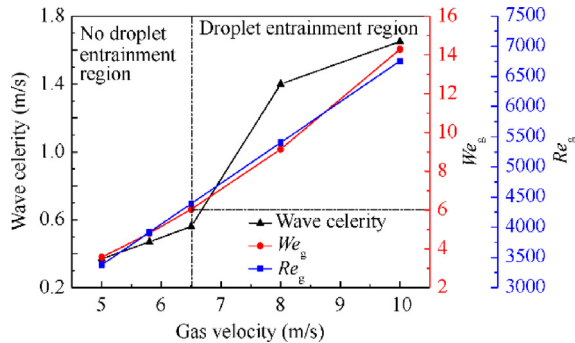


Fig. 11 Onset criteria for droplet entrainment in horizontal pipe.

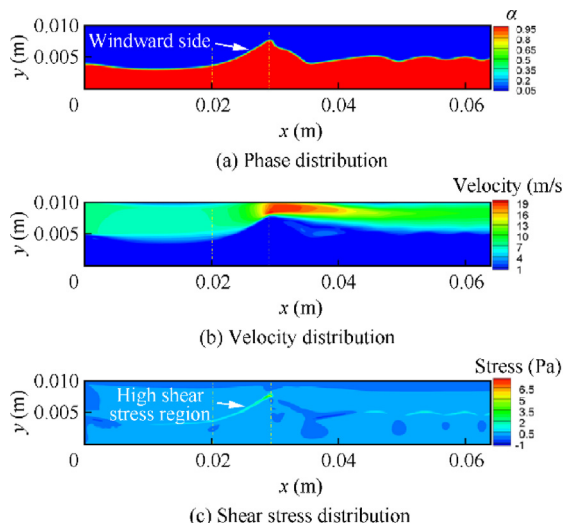


Fig. 12 Phase, velocity and shear stress contours (gas velocity: 7.2 m/s, $t = 0.105$ s).

strong, so liquid droplets can be generated more easily within this region. We_g , Re_g , shear stress from gas, and surface tension can be calculated by the following equations, respectively:

$$We_g = \frac{\rho_g u_g^2 D}{\sigma_f} \quad (14)$$

$$Re_g = \frac{\rho_g u_g D}{\mu_g} \quad (15)$$

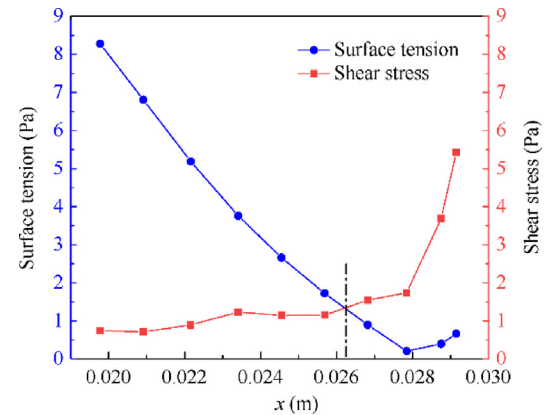


Fig. 13 Surface tension and shear stress distributions on contour line of.

$$\tau_g = \mu^* \left(\frac{du}{dy} + \frac{dv}{dx} \right) \quad (16)$$

$$\mu^* = \alpha \mu_f + (1 - \alpha) \mu_g \quad (17)$$

$$F_\sigma = \frac{\sigma_f}{R} \quad (18)$$

$$R = \left| \frac{(1 + y'^2)^{3/2}}{y''} \right| \quad (19)$$

where We_g is the Weber number of gas, Re_g is the Reynolds number of gas, ρ_g is the density of gas, u_g is the velocity of gas, D is the diameter of the tube, σ_f is the surface tension coefficient of liquid, μ_f is the dynamic viscosity of liquid, μ_g is the dynamic viscosity of gas, and R is the curvature radius.

The formation and development of wave have an obvious influence on the gas flow field structure, and the gas vorticity distribution is illustrated in Fig. 14.

It can be found that there are gas vortices above the liquid wave from Fig. 14, which is because the gas velocity near the interface is slower than that far away from the gas–liquid interface due to the friction force between gas and liquid. Besides, the intensity and range of vortices have a positive correlation with the size of wave. Thus, for further study of the relation between gas vortices and interfacial wave, the structures in Fig. 15 are calculated respectively, and results are shown in Fig. 16.

Figs. 16(a) and (b) show that inner spoilers can induce a gas vortex easily near the gas–liquid interface, leading to formation of interfacial waves. These waves are synchronous and similar due to the similar vortex. Besides, the wave formation time in Fig. 16(a) is shorter than that in Fig. 9(c), even under the same gas speed (6.5 m/s). Figs. 16(c) and (d) show that the vortex is mainly constrained to the outer spoiler, and there is no vortex near the gas–liquid interface, so waves are not formed and there is very little droplets entrainment. The windward side of wave is elongated by gas dragging in the direction of gas, and the leeward side of wave is subject to the vortex. The gas velocity and the strength of the vortex determine the scale of wave, and as a result, a wave is formed. The interaction between gas and liquid can be illustrated by Fig. 17.

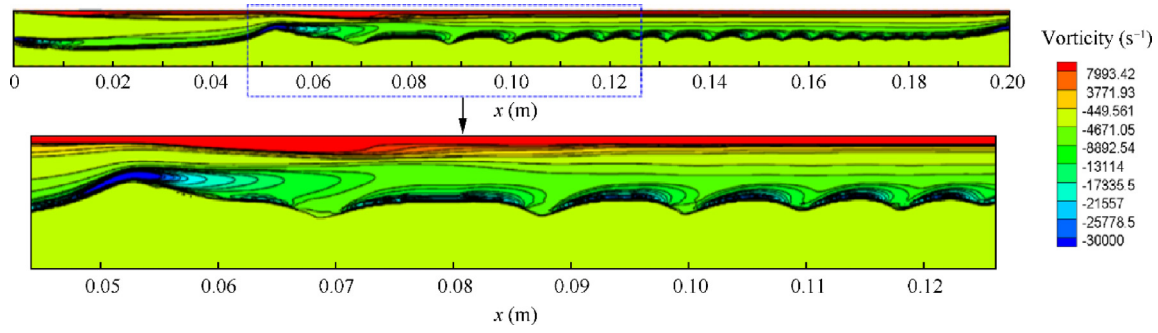


Fig. 14 Vorticity distribution (gas velocity: 6.5 m/s).

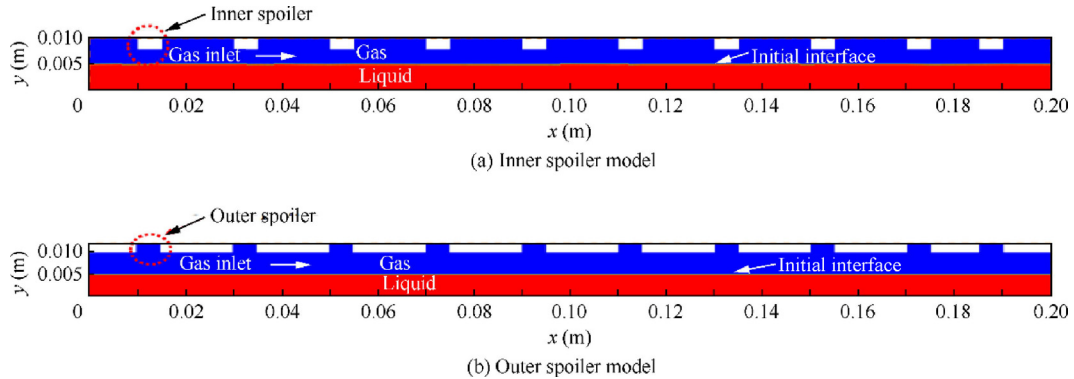


Fig. 15 Calculation models.

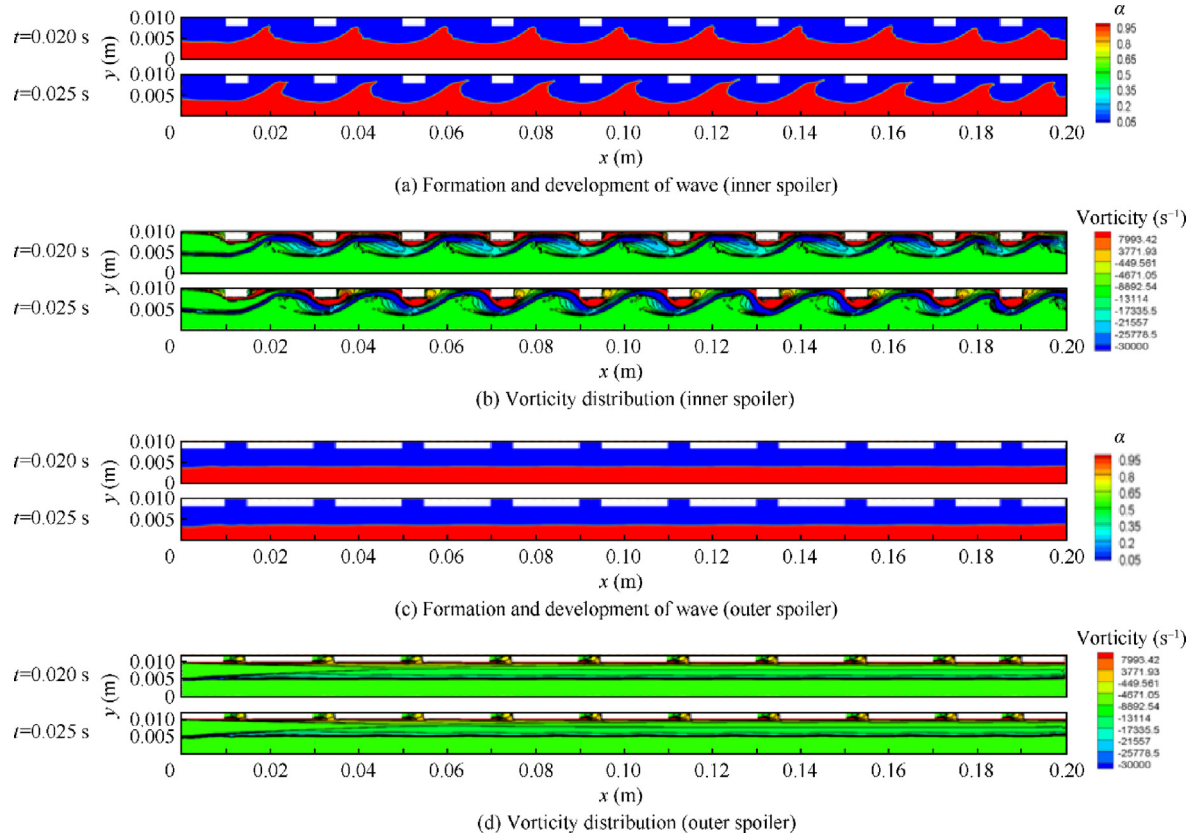


Fig. 16 Comparison of vorticity distributions of different structures (gas velocity: 6.5 m/s).

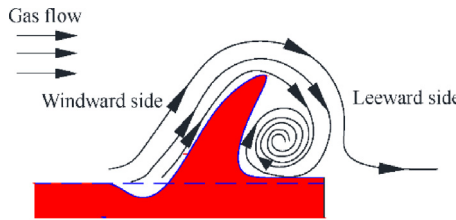


Fig. 17 Interaction between gas and liquid.

Based on the above analysis, the gas vortex plays an important role in wave formation and development. We can adjust wave formation and development through regulation of the gas vortex to some extent. Some measures of the regulation vortex can be taken to improve the stability of liquid film and depress the droplets entrainment rate in some industrial applications.

In order to investigate the development of father wave more intuitively, we can take Case 5 in Table 2 (gas velocity: 8.0 m/s) as an example, as shown in Fig. 18.

Fig. 18 shows that the wave develops slowly before 0.06 s, while the wave height increases dramatically from 0.06 s to 0.08 s. The windward profiles of father wave are shown in Fig. 19.

Fig. 19 shows that the windward side of father wave profile has a typical S-shape structure, and the wave height is the greatest at 0.075 s, then the top of wave is pressed down by the gas. In the beginning, the values of trough and crest are not equal, and the value of trough is greater than that of crest. However, the value of crest becomes greater than that of trough after 0.06 s. This is because the shear stress caused by gas becomes stronger near the crest. The influence of different gas velocities over the shape of father wave is shown in Fig. 20.

In Fig. 20(a), when the gas velocity is faster, it takes less time to reach maximum crest, and the shear stress grows greater. With growing shear stress, the wave height becomes higher, while the liquid is elongated more easily. As a result, the slope angle of the wave gets greater, which can be seen in Fig. 20(b). Fig. 20(b) also shows that the maximum slope angle usually does not exceed 38°, and the slope angle rises dramatically at first, then slowly, and then dramatically again when the gas velocity is between 6.5 m/s and 8.0 m/s, whereas others do not. Father wave develops rapidly with an increase

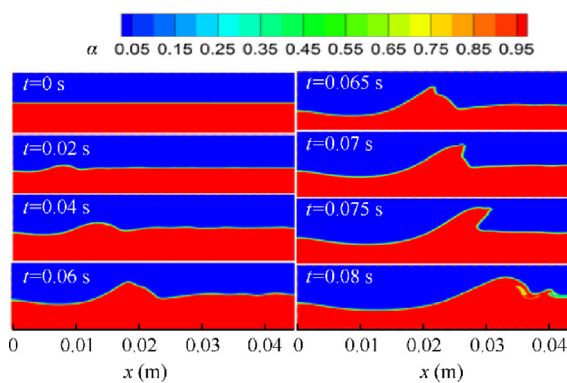


Fig. 18 Formation and development of father wave (gas velocity: 8.0 m/s).

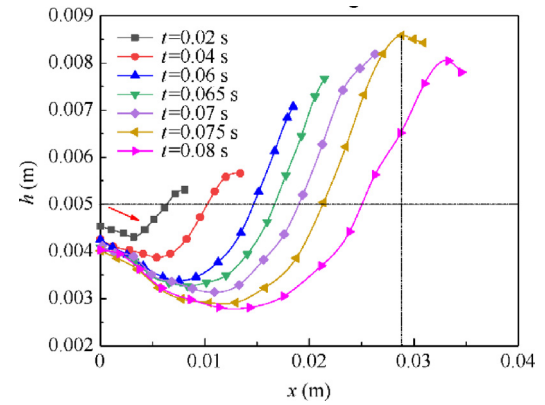
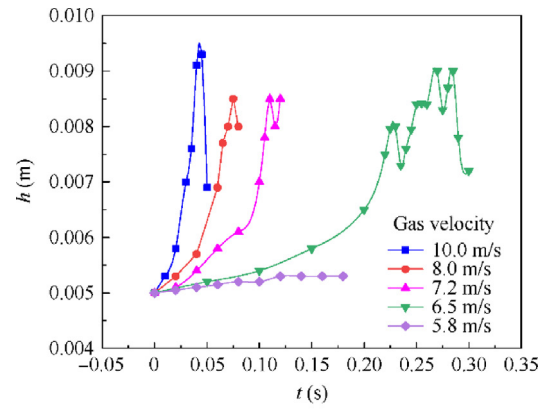
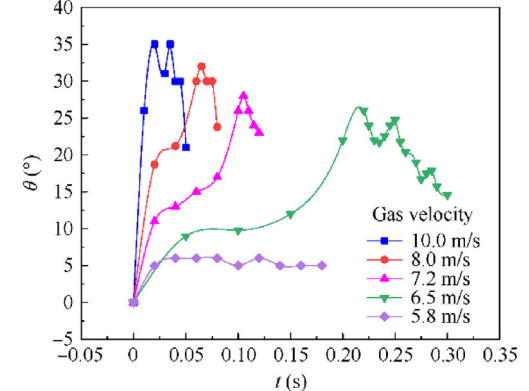


Fig. 19 Windward profiles of father wave (gas velocity: 8.0 m/s).



(a) h vs t



(b) θ vs t

Fig. 20 Shape parameters of wave at different gas velocities.

of the gas velocity, and the interaction between gas and liquid gets stronger.

The relations between the maximum wave height, the maximum slope angle and the gas velocity are shown in Fig. 21. It can be seen that the trends of the maximum wave height and maximum slope angle are similar, firstly increasing rapidly and then leveling off as the gas velocity increases. Father wave is firstly formed in the gas velocity ranging from 5.8 m/s to 6.5 m/s, which indicates that the gas–liquid interface is becoming unstable and droplets are generated. The wave height and slope angle gradually become stable when the gas velocity

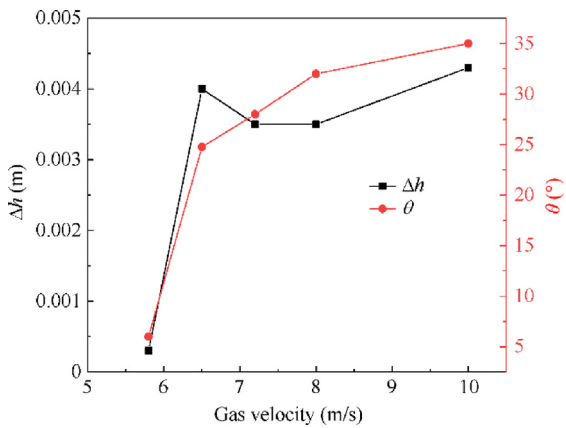


Fig. 21 Relations between the maximum slope angle, maximum wave height of father wave and different gas velocities.

exceeds 6.5 m/s. The droplets entrainment fraction levels off as the superficial gas velocity increases, as shown in Fig. 22.³⁴ It can be easily found that there is a similar distribution trend between Figs. 21 and 22. Besides, according to the droplets generation mechanism in this paper and Refs. 18,19,33, the wave height and slope angle play an important role in the droplets caused by the cutting off mode. The cutting off mode is dominant among the droplets generation modes.^{20,35} Consequently, it can be concluded that the distribution regularities of the maximum wave height and maximum slope angle should have a close relation with the variation of entrainment fraction. In gas–liquid two-phase flow, the droplet entrainment fraction is usually related to factors such as liquid surface tension coefficient, liquid dynamic viscosity, gas velocity, and liquid density, which play an important role in droplet generation. Although the maximum wave height, wave velocity, and maximum slope angle have an influence on droplet generation, it is difficult to evaluate the droplet entrainment fraction solely based on these parameters right now. More attentions need to be paid to the underlying relationship between these parameters and the droplet entrainment fraction in future work.

The superficial gas velocity can be calculated by the following equations:

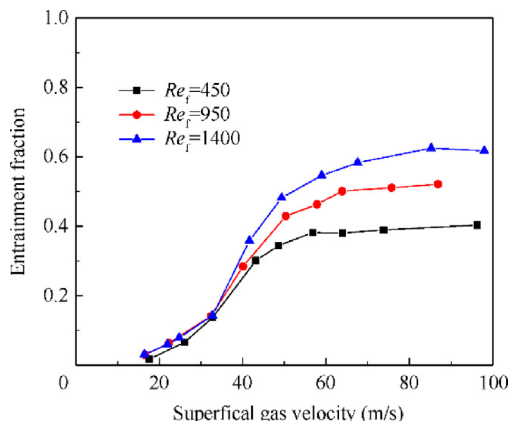


Fig. 22 Relation between entrainment fraction and superficial gas velocity under different liquid Reynolds numbers.³⁴

$$\langle j_g \rangle = \frac{Q}{A} \quad (20)$$

$$A = \frac{\pi D_{in}^2}{4} \quad (21)$$

where $\langle j_g \rangle$ is the superficial gas velocity, Q is the volume flow rate of gas, A is the cross-sectional area of the test pipe, and D_{in} is the inside diameter of the test pipe.

The actual gas velocity at the entrance of the test section can be obtained by

$$u_g = \frac{Q}{S} \quad (22)$$

where u_g is the actual gas velocity at the entrance of the test loop, and S is the actual area occupied by the gas phase at the entrance of the test loop.

Because the actual flow area S is hardly determined in an experiment,³⁴ the velocity of the gas phase u_g is difficult to be obtained, while it is easy to get the superficial gas velocity. Therefore, in Fig. 22, experimental results in the literature can be analyzed using the superficial gas velocity rather than the gas velocity.

4.2. Different surface tensions

To investigate the influence of the surface tension of liquid on interfacial wave, different surface tensions of liquid as in Table 4 were conducted in our research. The development process of interfacial wave is depicted under different surface tension coefficients in Fig. 23.

As can be seen from Figs. 23 and 24, it takes the shortest time to form and develop father wave when the surface tension coefficient is least. Meanwhile, the wave celerity increases as the surface tension coefficient decreases. The fluid is more easily dragged by gas when the surface tension decreases, which makes the interface become unstable, or even destroys the interface stability. Besides, there is an interesting phenomenon that the trough value increases with the surface tension decreasing, whereas the crest value of father wave firstly increases and then decreases, and the surface tension coefficient corresponding to the maximum wave height is 0.05 N/m in Fig. 25.

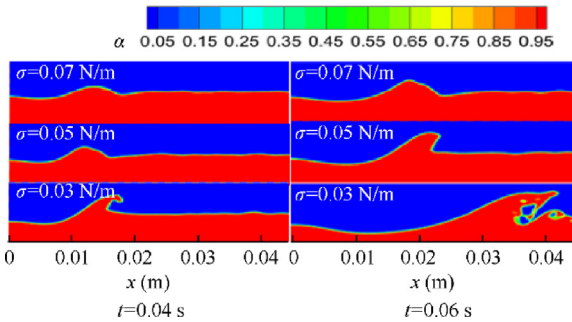
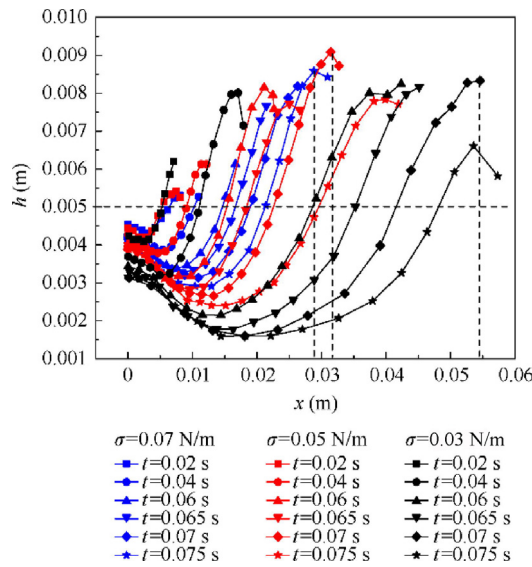
The slope angle of father wave is mainly distributed between 15° and 38° (Fig. 26). The maximum angle is corresponding to the minimum surface tension, which indicates that the suppression effect on liquid deformation is the weakest. From another aspect, it also shows that the surface tension has an obvious effect on the interfacial wave.

The relations between interfacial wave parameters and the surface tension coefficient are shown in Fig. 27. The slope angle of father wave decreases as the surface tension coefficient increases, while the height of father wave firstly increases and then decreases. This phenomenon indicates that the surface tension has a different effect on the profile of father wave at a different varying range of the surface tension coefficient. According to Fig. 27, the profile of father wave can be concluded as shown in Fig. 28.

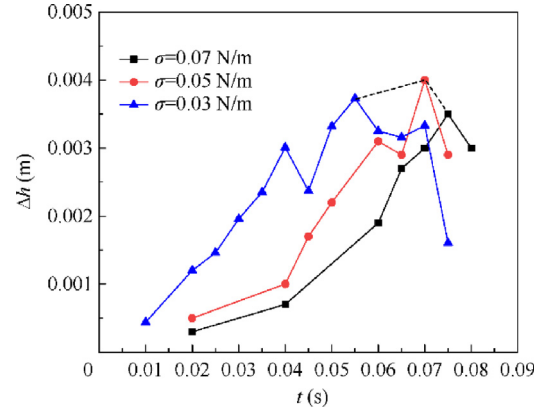
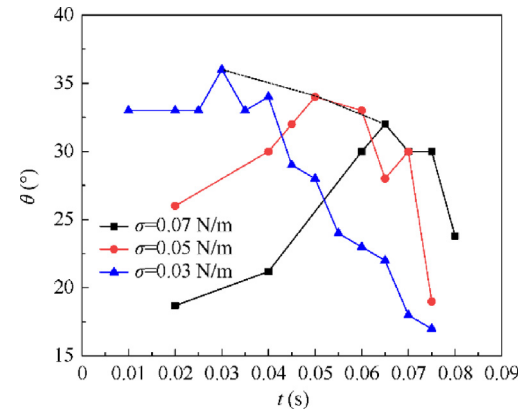
Fig. 28 shows that the profile of father wave becomes big and obvious as the surface tension increases in the range of 0.03 N/m to 0.05 N/m, while the volume of father wave becomes small and inconspicuous in the range of 0.05 N/m

Table 4 Different interfacial tensions.

Case	Item	Density (kg/m^3)	Viscosity (Pa·s)	Interfacial tension coefficient (N/m)
1	Gas(air)	1	1.48×10^{-5}	0.07
	Liquid(water)	1000	0.001	
2	Gas(air)	1	1.48×10^{-5}	0.05
	Liquid(water)	1000	0.001	
3	Gas(air)	1	1.48×10^{-5}	0.03
	Liquid(water)	1000	0.001	

**Fig. 23** Profiles of father wave at different moments under different surface tension coefficients (gas velocity: 8.0 m/s).**Fig. 24** Development process of interfacial wave under different surface tension coefficients (gas velocity: 8.0 m/s).

to 0.07 N/m. There is a value of surface tension coefficient corresponding to the biggest volume of father wave, and the gas–liquid interface is the most unstable at the moment. This value is about 0.05 N/m, which is named critical surface tension coefficient in this paper. When the surface tension coefficient is below the critical value, the liquid at the interface is dragged easily, and a small volume of liquid droplets will be generated. When the surface tension is above the critical value, the liquid

**Fig. 25** Relation between wave height and surface tension coefficient at different moments (gas velocity: 8.0 m/s).**Fig. 26** Relation between slope angle and surface tension coefficient at different moments (gas velocity: 8.0 m/s).

at the interface is hard to be dragged, and liquid droplets are difficult to be formed. Thus, we can depress the droplets entrainment by increasing the surface tension coefficient above 0.05 N/m.

4.3. Different viscosities

The influences from different viscosities of liquid on the characteristics of interfacial wave were investigated, and detailed parameters are shown in [Table 5](#).

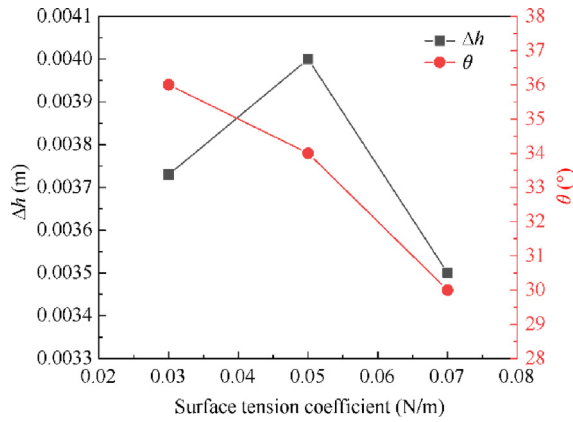


Fig. 27 Relations between the maximum slope angle, maximum height of father wave and surface tension coefficient (gas velocity: 8.0 m/s).

The profiles of father wave are shown in Fig. 29 at different moments, and the development process of interfacial father waves is depicted under different viscosities in Fig. 30.

From Figs. 29 and 30, the formation and development of father wave are the fastest when the liquid viscosity is the greatest. This phenomenon indicates that highly viscous liquid can drag the fluid under the interface to flow in the direction of gas more easily. In other words, highly viscous fluid is easier to be elongated, which will cause two results, one is that the wave height is the highest and the other is the phenomenon of liquid cutting off firstly occurs. Thus, the viscosity of liquid has a positive effect on the formation and development of interfacial wave. The height and slope angle of father wave are illustrated in Figs. 31 and 32, respectively.

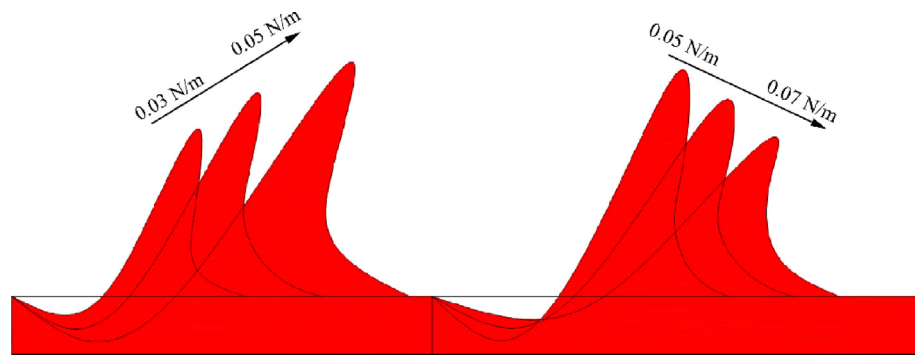


Fig. 28 Profiles of father wave under different ranges of surface tension coefficient.

Table 5 Different viscosities of liquid.

Case	Item	Density (kg/m ³)	Viscosity (Pa·s)	Interfacial tension coefficient (N/m)
4	Gas(air)	1	1.48×10^{-5}	0.07
	Liquid(water)	1000	0.001	
5	Gas(air)	1	1.48×10^{-5}	0.07
	Liquid(water)	1000	0.004	
6	Gas(air)	1	1.48×10^{-5}	0.07
	Liquid(water)	1000	0.008	

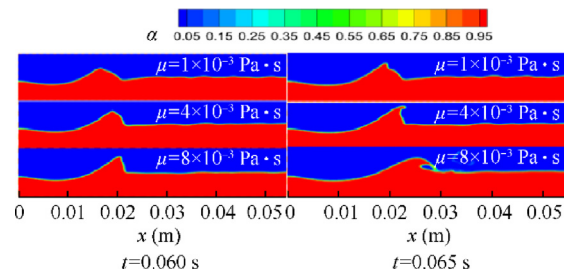


Fig. 29 Profiles of father wave at different moments under different viscosities (gas velocity: 8.0 m/s).

Fig. 31 shows that there is a positive correlation between the wave height and viscosity. The greater the liquid viscosity, the higher its wave height, which is due to that the viscosity of liquid can prevent the liquid from blowing away. It is conducive to continuous accumulation of liquid and wave formation. Fig. 32 shows that there is still a positive correlation between the maximum slope angle and the dynamic viscosity, and the maximum slope angle is about 35°. Meanwhile, there is an interesting phenomenon that the slope angle of liquid with a low dynamic viscosity is greater than that of liquid with a high dynamic viscosity in the beginning, while the slope angle growth rate of high-viscosity liquid is greater than that of low-viscosity liquid as time goes on. The greater the liquid viscosity, the greater the maximum slope angle of father wave.

The relations between the maximum wave height, maximum slope angle and the dynamic viscosity are shown in Fig. 33. The wave height and slope angle are positively correlated with the liquid viscosity. The wave height begins to level off as the dynamic viscosity increases, while the windward

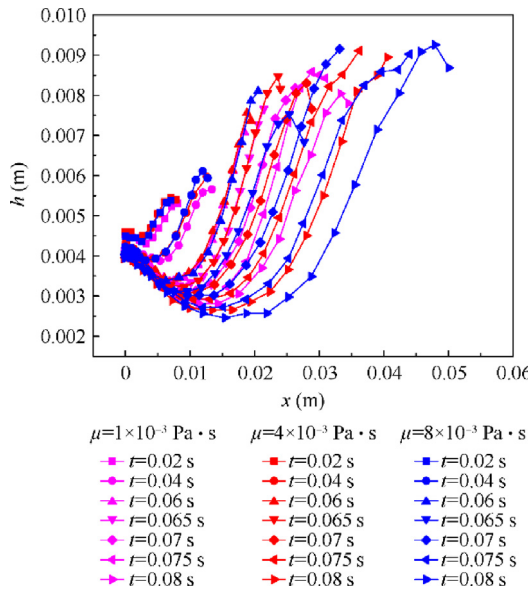


Fig. 30 Development process of interfacial wave under different viscosities (gas velocity: 8.0 m/s).

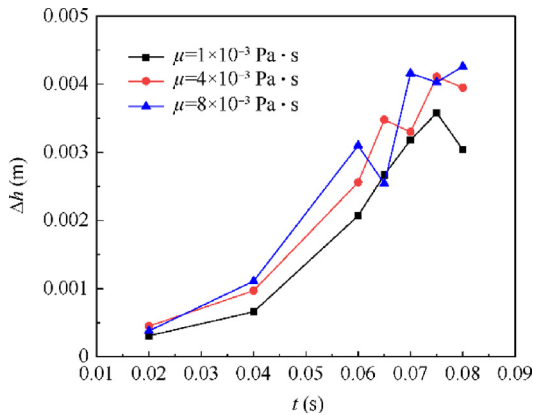


Fig. 31 Relation between wave height and different dynamic viscosities at different moments (gas velocity: 8.0 m/s).

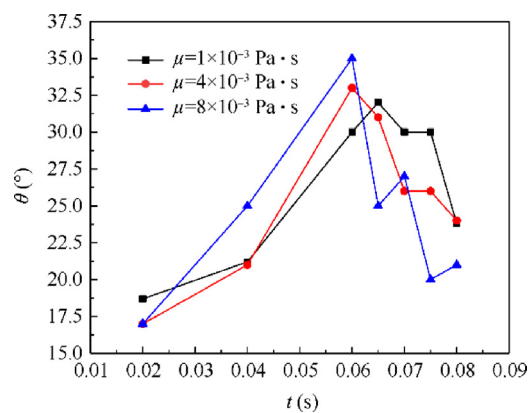


Fig. 32 Relation between slope angle and different dynamic viscosities at different moments (gas velocity: 8.0 m/s).

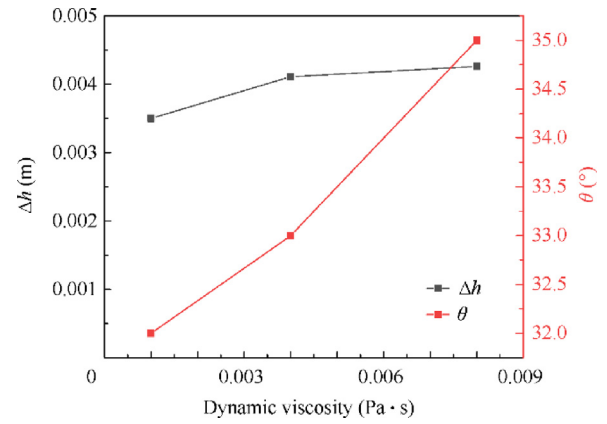


Fig. 33 Relations between maximum wave height, maximum slope angle and dynamic viscosity (gas velocity: 8.0 m/s).

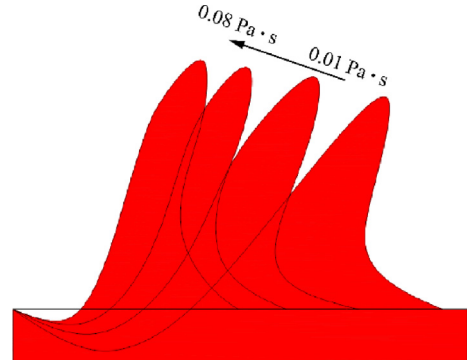


Fig. 34 Profiles of father wave under different dynamic viscosities.

slope angle increases gradually as shown in Fig. 34. The influence from the dynamic viscosity on wave formation and development is positive, while that of the surface tension is negative, and thus the two factors have different effects on the wave.

5. Conclusions

Numerical simulations were conducted to investigate the characteristics of interfacial wave in a horizontal gas-fluid pipe using OpenFOAM, the mechanism of formation and development of interfacial wave was revealed and illustrated, and four modes of droplet entrainment were found in this process. Besides, the influences from the gas momentum, the surface tension coefficient and viscosity of liquid on interfacial wave were investigated respectively. Some important conclusions were obtained in present study as follows.

- (1) The gas momentum is critical to the formation and development of interfacial wave in gas-fluid flow. The liquid at the interface will be piled up, lifted, and elongated to form a finger shape under gas dragging. Besides, father wave is formed firstly, followed by son waves. Father wave directly determines the stability of downstream interfacial wave, which is important to study gas-liquid flow.

- (2) The droplets entrainment mechanism is revealed intuitively, and four modes coexist in actual gas–liquid flow, which are cutting off from gas, hitting from the wave body, droplets impingement, and bubbles burst, respectively. These modes make the entrainment process very complicated, which causes a challenge to predict the droplet entrainment rate accurately. The gas vortex has an obvious influence on the formation and development of interfacial wave, and the regulation of vortex can be used to depress the droplets entrainment rate and improve the liquid film stability.
- (3) Interfacial wave is gradually formed in the range of $Re_g = 3378 - 4400$, but there is no entrainment in this range. The entrainment occurs when Re_g is above 4400, and the entrainment rate grows as the gas velocity increases. However, the maximum height and maximum slope angle of wave will level off after $Re_g = 5500$. Besides, the maximum slope angle of wave is usually no more than 38° .
- (4) The surface tension and viscosity have different effects on the formation and development of interfacial wave. The surface tension has a negative effect above the critical surface tension coefficient, and the viscosity has a positive effect. In order to depress the phenomenon of entrainment and improve the stability of liquid film, increasing the surface tension above the critical surface tension coefficient and decreasing the viscosity of liquid can be applied.

Declaration of Competing Interest

The authors declare that they have no known competing financial interests or personal relationships that could have appeared to influence the work reported in this paper.

References

- Arnold R, Suslov DI, Haidn OJ. Film cooling in a high-pressure subscale combustion chamber. *J Propul Power* 2010;26(3):428–38.
- Ekkad SV, Han JC. Film cooling measurements on cylindrical models with simulated thermal barrier coating spallation. *J Thermophys Heat Transfer* 2000;14(2):194–200.
- Höglauer C, Kriesner B, Knab O, et al. Modeling and simulation of a GOX/kerosene subscale rocket combustion chamber with film cooling. *CEAS Space J* 2015;7(4):419–32.
- Jang D, Kwak Y, Kwon S. Design and validation of a liquid film-cooled hydrogen peroxide/kerosene bipropellant thruster. *J Propul Power* 2015;31(2):761–5.
- Cao N, Li X, Wu ZY, et al. Effect of film hole geometry and blowing ratio on film cooling performance. *Appl Therm Eng* 2020;165:114578.
- Bills JD, Crowe DS, Rutledge JL, et al. Modeling fuel film cooling on a flat plate. *J Thermophys Heat Transfer* 2018;32(3):736–46.
- He K, Li JJ, Yan X. Numerical investigations into heat transfer and film cooling effect on a transonic blade endwall. *Appl Therm Eng* 2018;129:934–52.
- Javadi K. Introducing film cooling uniformity coefficient. *Heat Transf Eng* 2018;39(2):180–93.
- Jiang YT, Yue GQ, Dong P, et al. Investigation on film cooling with swirling coolant flow by optimizing the inflow chamber. *Int Commun Heat Mass Transf* 2017;88:99–107.
- Bae B, Ahn T, Jeong J, et al. Characteristics of an interfacial wave in a horizontal air-water stratified flow. *Int J Multiph Flow* 2017;97:197–205.
- Bae B, Kim T, Jeong J, et al. Droplet entrainment and deposition rates in a horizontal annular flow for SPACE code. *Prog Nucl Energy* 2018;109:45–52.
- Berna C, Escrivá A, Muñoz-Cobo JL, et al. Review of droplet entrainment in annular flow: Interfacial waves and onset of entrainment. *Prog Nucl Energy* 2014;74:14–43.
- Cioncolini A, Thome JR. Prediction of the entrained liquid fraction in vertical annular gas-liquid two-phase flow. *Int J Multiph Flow* 2010;36(4):293–302.
- Cuadros JL, Rivera Y, Berna C, et al. Characterization of the gas-liquid interfacial waves in vertical upward co-current annular flows. *Nucl Eng Des* 2019;346:112–30.
- He H, Liu XJ, Pan QQ, et al. Experimental and theoretical study on formation of interfacial waves on liquid film of annular two-phase flow. *Nucl Eng Des* 2022;389:111683.
- Rivera Y, Berna C, Muñoz-Cobo JL, et al. Experiments in free falling and downward cocurrent annular flows - Characterization of liquid films and interfacial waves. *Nucl Eng Des* 2022;392:111769.
- Wijayanta S, Prasetyo A, Hudaya AZ. The effect of the liquid physical properties on the wave frequency and wave velocity of co-current gas-liquid stratified two-phase flow in a horizontal pipe. *Int J Multiph Flow* 2023;158:104300.
- Liu L, Bai BF. Generalization of droplet entrainment rate correlation for annular flow considering disturbance wave properties. *Chem Eng Sci* 2017;164:279–91.
- Ryu SH, Park GC. A droplet entrainment model based on the force balance of an interfacial wave in two-phase annular flow. *Nucl Eng Des* 2011;241(9):3890–7.
- Holowach MJ, Hochreiter LE, Cheung FB. A model for droplet entrainment in heated annular flow. *Int J Heat Fluid Flow* 2002;23(6):807–22.
- Rana BK, Das AK, Das PK. Numerical study of air entrainment and liquid film wrapping around a rotating cylinder. *Ind Eng Chem Res* 2016;55(46):11950–60.
- Stel H, Ofuchi EM, Chiva S, et al. Numerical assessment of performance characteristics and two-phase flow dynamics of a centrifugal rotor operating under gas entrainment condition. *Exp Comput Multiph Flow* 2022;4(3):221–40.
- Ramadan Z, Park CW. Numerical investigation of gas-liquid slug formation in T-junction microchannel using OpenFOAM. *Chem Pap* 2021;75(8):4381–90.
- Höhne T, Hänsch S. A droplet entrainment model for horizontal segregated flows. *Nucl Eng Des* 2015;286:18–26.
- Berberovic E. Investigation of free-surface flow associated with drop impact: Numerical simulations and theoretical modeling [dissertation]. Darmstadt: Darmstadt University of Technology; 2010.
- Liu Q, Gómez F, Pérez JM, et al. Instability and sensitivity analysis of flows using OpenFOAM®. *Chin J Aeronaut* 2016;29(2):316–25.
- Tao WQ. *Numerical heat transfer*. 2nd ed. Xi'an: Xi'an Jiaotong University Press; 2004. p. 90–8 [Chinese].
- Sweby PK. High resolution schemes using flux limiters for hyperbolic conservation laws. *SIAM J Numer Anal* 1984;21(5):995–1011.
- Leonard BP. Simple high-accuracy resolution program for convective modelling of discontinuities. *Int J Numer Meth Fluids* 1988;8(10):1291–318.
- Aleksenko SV, Cherdantsev AV, Heinz OM, et al. Analysis of spatial and temporal evolution of disturbance waves and ripples in annular gas-liquid flow. *Int J Multiph Flow* 2014;67:122–34.
- Wang K, Bai BF, Ma WM. A model for droplet entrainment in churn flow. *Chem Eng Sci* 2013;104:1045–55.

32. Belt RJ, Van't Westende JMC, Prasser HM, et al. Time and spatially resolved measurements of interfacial waves in vertical annular flow. *Int J Multiph Flow* 2010;36(7):570–87.
33. Mantilla I. Mechanistic modeling of liquid entrainment in gas in horizontal pipes [dissertation]. Tulsa: University of Tulsa; 2008.
34. Sawant P, Ishii M, Mori M. Droplet entrainment correlation in vertical upward co-current annular two-phase flow. *Nucl Eng Des* 2008;238(6):1342–52.
35. Kataoka I, Ishii M, Nakayama A. Entrainment and desposition rates of droplets in annular two-phase flow. *Int J Heat Mass Transf* 2000;43(9):1573–89.